RSC Applied Interfaces

ROYAL SOCIETY OF CHEMISTRY

PAPER

View Article Online
View Journal | View Issue

Check for updates

Cite this: *RSC Appl. Interfaces*, 2024, 1, 492

Solution treatment controls charge-transfer states and energy-level alignment at hybrid CuSCN-organic interfaces†

Yingying Li,[ab] Zhewei Chen,[ab] Wenjie Zhou,[ab] Qi Wang,[ab] Yuan Zhang,[ab] Tao Song,*[ab] Baoquan Sun*[ab] and Steffen Duhm*[ab]

Received 6th December 2023,
Accepted 22nd January 2024

DOI: 10.1039/d3lf00244f

rsc.li/RSCApplInter

Hybrid organic–inorganic optoelectronic devices combine the advantages of both material classes. However, efficient formation of emissive charge-transfer (CT) states at organic–inorganic interfaces is rarely observed. A notable exception is the copper thiocyanate (CuSCN)-organic interface, which might be due to the molecular and defect-rich nature of CuSCN films. We show that the treatment of CuSCN–diethyl sulfide (DES) solution by heating and/or filtration has an eminent impact on the morphology of CuSCN films and by optimizing the thin film preparation the CT-state formation at CuSCN-organic interfaces can be significantly increased. This is brought about by CuSCN–DES coordination (as evidenced by X-ray photoelectron spectroscopy) and the decrease of charge trapping states. Furthermore, the valence electronic structure was measured by ultraviolet photoelectron spectroscopy and the energy-level alignment at the interface of the CuSCN layer with the highest CT-state intensity and C_{60} interfaces is most favorable for efficient charge transport across the interface. Overall, our insight in CT-state formation efficiency at the inorganic–organic interface paves the way for further applications of CuSCN in hybrid electronic devices.

Introduction

Hybrid inorganic–organic heterojunctions have attracted intense interest from the optoelectronic research community in recent years as they offer the possibility to combine the advantages of both materials.[1–5] These are, in particular, the high absorption coefficients over a wide wavelength range and facile solution processability of most organic semiconductors and the high stability, carrier mobility, and crystallinity of inorganic semiconductors.[6,7] However, a notoriously low efficiency of photoexcited charge transfer (CT) at organic–inorganic interfaces hampers their direct application in high-performance photovoltaic devices.[8,9] Interfaces of copper thiocyanate (CuSCN) with organic materials are notable exception and recently the formation of CT states at such interfaces has been directly proven by the observation of its nonradiative recombination in electroluminescence (EL).[2] Furthermore, solution-processable CuSCN is readily available at low costs to fabricate thin films with a high hole mobility,[10–12] and suitable energy levels that allow efficient hole injection/extraction while simultaneously blocking electron transport.[13,14] CuSCN combines p-type semiconductor characteristics with a large energy band gap and a large electron affinity, which can form type II heterojunctions with many organic materials.[10,15,16] Consequently, CuSCN has so far been successfully applied as hole transporting material in organic light-emitting diodes (OLEDs),[17,18] thin film transistors (TFTs),[10] and photovoltaic devices.[19–21]

In contrast to inorganic–organic interfaces, efficient CT state formation is frequently observed at the donor–acceptor interface in organic photovoltaics[22–24] and the dielectric medium plays an important role in this process.[25] In general, electrostatically bound organic semiconductors have much lower dielectric constants (2–3) than chemically bound inorganic semiconductors (10–15), which results in localized Frenkel excitons rather than delocalized Wannier–Mott excitons.[26] For the inorganic, yet molecular material CuSCN dielectric constant values of 3.5 (ref. 10) and 5.1 (ref. 12) were reported and such a spread can be expected as the solvent and the preparation steps have an eminent impact on the properties of solution-processed, defect-rich thin films.[27,28] Various solvents have been used for CuSCN thin film

[a] *Institute of Functional Nano & Soft Materials (FUNSOM), Soochow University, Suzhou 215123, People's Republic of China. E-mail: tsong@suda.edu.cn, bqsun@suda.edu.cn, duhm@suda.edu.cn*

[b] *Jiangsu Key Laboratory of Advanced Negative Carbon Technologies, Soochow University, Suzhou 215123, People's Republic of China*

† Electronic supplementary information (ESI) available: Current–voltage characteristics, scanning-electron microscopy images, additional photoelectron spectroscopy and atomic force microscopy data. See DOI: https://doi.org/10.1039/d3lf00244f

Table 1 Solution treatment methods and properties of CuSCN films on PEDOT:PSS/ITO

	Solution treatment	VBM (eV)	Rel. CT-state intensity	Trap states (cm^{-3})
#xx	Untreated	0.90	1.9	3.54×10^{17}
#Hx	Heated	0.87	0.9	3.51×10^{17}
#xF	Filtrated	0.79	10.6	2.73×10^{17}
#HF	Heated, filtrated	0.86	2.1	3.34×10^{17}

preparation[29–32] and diethyl sulfide (DES) has evolved as most common solvent, because it has an enhanced solubility compared to other solvents, which significantly improves the continuity and uniformity of the deposited film.[13,33] Furthermore, DES can coordinate with Cu(I) which plays an important role in controlling the microstructure of CuSCN films and ultimately affects the hole transport properties.[34–36] The coordination involves a rather large amount of CuSCN (around 20% as shown by X-ray absorption spectroscopy),[35] and this organic component in CuSCN films might be beneficial for the CT state formation at the CuSCN/organic interface.

Overall, despite the promising results, a basic understanding of the mechanisms of CT states formation at CuSCN/organic interfaces is still lacking, which needs to be thoroughly investigated to expend the application of CuSCN in hybrid devices. In this study, we report the impact of the solution treatment method on the structural, optical, and electronic properties of spin-coated CuSCN films. We show by means of atomic force microscopy (AFM) and X-ray diffraction (XRD) that solution filtration has an eminent impact on the morphology and increases the crystallinity of the thin films. In contrast, the coordination of the DES solvent with CuSCN, as revealed by X-ray photoelectron spectroscopy (XPS), and the optical absorption spectra measured by UV/vis spectroscopy, is rather independent of the solution treatment method. EL measurements at CuSCN/C_{60} interfaces reveal a strong dependence of the CT state intensity on the solution treatment method, while ultraviolet photoelectron spectroscopy (UPS) shows that the ionization energies (IEs) of the CuSCN films do not strongly depend on the solution treatment. Furthermore, the energy-level alignment at C_{60}/CuSCN interfaces was determined by UPS measurements of step-by-step deposited C_{60} on CuSCN. Finally, the interfacial defect density was accessed by transport measurements.

Results and discussion

Four solution treatment methods were employed to fabricate CuSCN films with a nominal thickness of 70 nm on indium-tin oxide (ITO) substrates: processing at room temperature (CuSCN #xx), heating of the solution to 60 °C (CuSCN #Hx), filtration of the solution (CuSCN #xF), and heating and filtration (CuSCN #HF); the acronyms are summarized in Table 1. All other parameters (solution concentration, spin-coating speed, annealing temperature of the thin films *etc.*) were kept the same and the detailed information about sample preparation can be seen in the Methods section.

Fig. 1a presents the AFM-measured surface topography of the CuSCN thin films. The thin film spin-coated from untreated solution (CuSCN #xx) exhibits uneven round-like features and the root-mean-square (RMS) of the surface roughness is 6.81 nm. Heating the solution (CuSCN #Hx) reduces the surface roughness (RMS of 4.21 nm) without notable changes to the surface aggregation. Filtering the solution (CuSCN #xF and #HF) transforms the grains into relatively dense elongated features such as oval/rod-like shapes. Interestingly, additional heating of the filtered solution does not notably affect the surface roughness (RMS of 5.84 nm and 5.37 nm for CuSCN #xF and #HF, respectively). The XRD features (Fig. 1b) can be assigned to the (003), (101), and (006) peaks of the hexagonal β-CuSCN phase.[16] The Bragg peak positions are rather identical for each film, indicating that the crystal structure is not affected

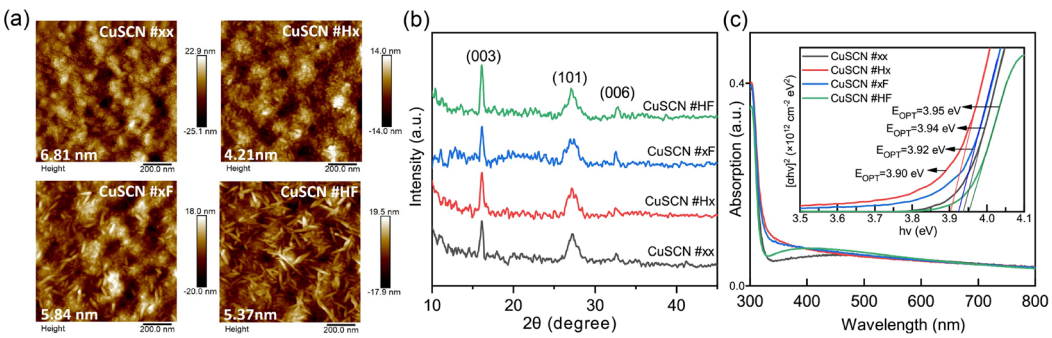

Fig. 1 (a) AFM topography of spin-coated CuSCN films on ITO with their respective surface roughness. (b) XRD patterns of CuSCN films on ITO (c) UV/vis absorption spectra of spin-coated CuSCN films on quartz; the inset shows the Tauc plots which were used to determine the optical gaps (E_{OPT}).

by the solution treatment methods. A high optical transparency is a key merit of CuSCN and the optical absorption spectra of CuSCN films on quartz (Fig. 1c) are not affected by the solution treatment method. In particular, all four CuSCN thin films are extremely transparent in the visible to near-infrared region and the absorption onset is in the ultraviolet at around 300 nm. The absorption data were used to extract the optical gap (E_{OPT}) by Tauc plots (inset in Fig. 1c) and the direct gaps of 3.90 eV to 3.95 eV are consistent with previous experimental and theoretical values.[16,37–39]

The chemical states of the elements in CuSCN were assessed by XPS and the core-level spectra are displayed in Fig. 2a and b (C 1s and N 1s) and Fig. S1† (Cu 2p and S 2p). The main peak in the N 1s spectra is centered at 398.3 eV binding energy (BE) and can be assigned to SCN bonds and the BE (399.6 eV) of the additional small feature is in the range of NH or CN bonds.[40,41] The peak dominating the C 1s core levels at 285.7 eV BE can be also assigned to SCN bonds[40] while the two further peaks at 283.7 eV BE and at 284.5 eV BE are in the typical BE-range of adventitious carbon.[42] The main peak of the Cu 2p core level spectrum at 932.6 eV BE corresponds to Cu(I)[43] and the S 2p spectrum shows a single doublet with the $2p_{3/2}$ peak centered at 163.0 eV BE, corresponding to SCN bonds.[40,41] Overall, the BE positions of all peaks do not notably depend on the solvent treatment method, which is in good agreement with previous XPS data of CuSCN films.[10,16,44–46] The high BE component in the N 1s spectrum was assigned to CN or NCS bonds[10,44] and the low BE component in the C 1s spectrum to adventitious carbon. In our work, all preparation steps were performed in a N_2-filled glove box and a likewise N_2-filled box was used for transport of the CuSCN films to the ultra-high vacuum chamber for XPS measurements, which ruled out adventitious carbon as main source for the low BE peaks in the C 1s spectra. In principle, these features could also stem from solvent residues but the S 2p spectra (Fig. S1b†) show no signs of a CS contribution, which would be expected in DES. This is in accordance with previous XPS data and was explained by the coordination of a large amount of CuSCN with DES.[35] We refrain from a quantification of CuSCN–DES coordination by the area ratio of the respective C 1s peaks as a small contamination by adventitious carbon cannot be completely excluded. Furthermore, the mean-free path of the photoelectrons in our experiment is around 10 nm (ref. 47) and this surface-sensitivity would lead to an overestimation of the DES content, as CuSCN–DES coordination mainly takes place at the surface of the crystallites.[35]

Fig. 2c shows the UPS-measured valence band region of the CuSCN films and for each spectrum the valence band maximum (VBM) is marked. The VBM of CuSCN #xF is at 0.77 eV below the Fermi level (E_F), which is shallower than that of the others (CuSCN #xx: 0.83 eV, CuSCN #Hx: 0.89 eV, CuSCN #HF: 0.84 eV) and indicates that the hole injection barrier between ITO and CuSCN #xF is the smallest. Fig. 2d shows the secondary electron region of the UPS spectra. The secondary electron cutoff (SECO) gives the position of the vacuum level (VL) with respect to E_F.[48] For all thin films the VL is at around 5.40 eV, confirming the p-type nature of the CuSCN thin films, which is due to the non-stoichiometry (Cu defects) of the solution-processed film.[49,50] The small differences in VL by the solution treatment method are attributed to the variation in the surface morphology and preferred orientation of the CuSCN films. The sum of VBM and VL corresponds to the IE of the thin films and no significant change upon different solution treatments can be observed. Fig. 2e shows the valence band spectra on a log-scale intensity. All four thin films exhibit band tails states with an onset at about 0.35 eV below E_F. This density of states (DOS) arises from Cu vacancies leading to an acceptor-like state above the VBM,[33,51,52] which could extend to E_F due to their broad energetic distribution.[16,53] In our UPS data, the

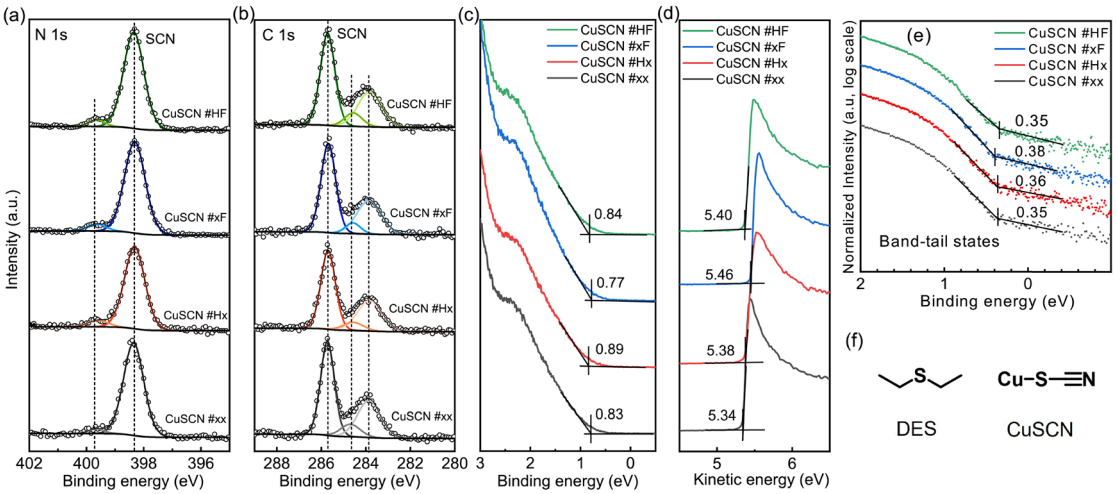

Fig. 2 XPS-measured (a) N 1s and (b) C 1s spectra of CuSCN films on ITO. UPS-measured (c) valence band region, (d) secondary electron, and (e) valence band regions plotted on a semi-log scale of CuSCN films on ITO. (f) Chemical structures of DES and CuSCN.

onset of the gap states is independent of the solution treatment method and a similar onset was observed in a previous UPS study.[51] These gap states lead to effective Fermi-level pinning[54–56] of the CuSCN films and provide, furthermore, a transport pathway for charge carriers, which is often termed mobility edge.[57]

To investigate the CT states at C_{60}/CuSCN heterojunctions, we fabricated EL devices with the structure of ITO/poly(3,4-ethylenedioxythiophene):poly(styrenesulfonate) (PEDOT:PSS) (30 nm)/CuSCN/C_{60}/bathocuproine (BCP) (10 nm)/Al (100 nm). The schematic device structure and normalized EL spectra are shown in Fig. 3. The reference device without the CuSCN layer shows an EL peak at ~1.67 eV, which originates from the excitonic emission of C_{60}, which is consistent with previous studies.[2,58] Devices with CuSCN layer show another peak centered at ~1.19 eV, which corresponds to light emission due to the CT state at the C_{60}/CuSCN interface through carrier recombination.[59,60] The EL peak of CT states does not show a significant shift among all the samples with CuSCN films obtained by different solution treatment method, indicating the same energy diagram of CT states in these devices. However, the EL intensity of the CT state with the CuSCN #xF layer is much higher compared to the other three samples in the normalized EL spectra. This enhanced EL emission of CT states in CuSCN #xF devices demonstrates more efficient charge transport and conversion of electrical charges at the inorganic–organic interface. To further explain

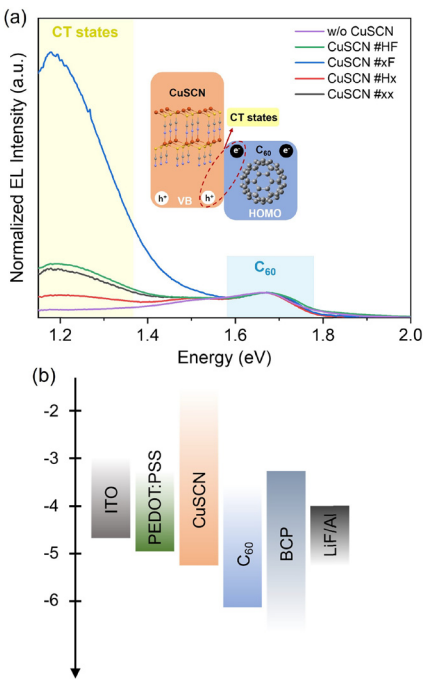

Fig. 3 (a) Normalized EL spectra of LED devices without CuSCN (purple line, based on PEDOT:PSS/C_{60}) and devices with a C_{60}/CuSCN heterojunction under different CuSCN conditions; the inset shows the schematic illustration of the CT state formation. (b) Energy-level diagram of the device structure assuming VL-alignment across the heterojunction.

this, hole-only devices with an architecture of ITO/PEDOT:PSS/CuSCN/C_{60}/MoO_x/Ag were fabricated to quantitatively study the carrier injection in the CuSCN films. According to the space-charge-limited current (SCLC) model, the linear change of current at low bias voltage can be considered as an Ohmic-type response, while the steep rise of current at high bias voltage is the trap-filling region. The trap density (N_t) can be determined by the trap-filled-limit voltage (V_{TFL}):[61]

$$N_t = \frac{2V_{TFL}\varepsilon\varepsilon_0}{qL^2} \quad (1)$$

where ε represents the relative dielectric constant, ε_0 is the vacuum permittivity, q is the elementary charge, and L is the thickness of the functional films. The V_{TFL} can be determined by fitting the I–V curve of the hole-only devices as shown in Fig. S4† and by using ε = 5.1 (ref. 12) the average N_t values are 3.54 × 10^{17} cm^{-3} (CuSCN #xx), 3.52 × 10^{17} cm^{-3} (CuSCN #Hx), 2.73 × 10^{17} cm^{-3} (CuSCN #xF) and 3.34 × 10^{17} cm^{-3} (CuSCN #HF), respectively. This illustrates that the CuSCN #xF-based device presents the lowest defect density and is, thus, most favorable for carrier injection. We note that these values are rough estimates as ε of our CuSCN films is unknown and, furthermore, ε of each individual CuSCN is not necessarily the same.

The trap-state density and the intensity of the CT state (relative to the EL peak of C_{60}) of the CuSCN films are shown in Table 1. For the device measurements CuSCN was spin-coated on PEDOT:PSS/ITO while pristine ITO was used for the basic characterization of the CuSCN films. In general, PEDOT:PSS has a lower surface roughness and a higher work function than ITO, which could impact the CuSCN properties. Indeed, the surface roughness of the CuSCN films on PEDOT:PSS/ITO (Fig. S2†) is slightly lower than on ITO (Fig. 1a), in particular for the non-filtrated samples. However, the electronic structure as measured by UPS is almost independent of the substrate (ITO, Fig. 2c–e and PEDOT:PSS/ITO, Fig. S3†). This confirms that the energy-level alignment is indeed controlled by the gap states and, consequently, independent of the substrate properties.[62] The properties of CuSCN films on ITO and on PEDOT:PSS/ITO are compared in the Table S1† and show that the impact of the substrate is rather low.

To get further insight in the charge-transfer characteristics at the CuSCN/C_{60} interface, we measured photoemission data of stepwise vacuum-sublimed C_{60} on spin-coated CuSCN and the data with the #xF layer is shown in Fig. 4. The intensity of the CuSCN valence band decreases with increasing C_{60} coverage, meanwhile, the intensity of the emission from C_{60} levels increases (Fig. 4a). The two peaks centered at 1.72 eV BE and 3.10 eV BE can be assigned to the highest occupied molecular orbital (HOMO) level and the HOMO-1 level of C_{60}, respectively. Their high intensity, which is due to the multiple degeneracy of these molecular orbitals,[63,64] and their BE-positions are in agreement with previous UPS reports of C_{60} films.[63,65] There is no significant thickness-dependent shift of the HOMO position. For a thickness of 128 Å the onset of the HOMO-level is at 1.24 eV BE (for smaller C_{60} coverages the determination of the onset

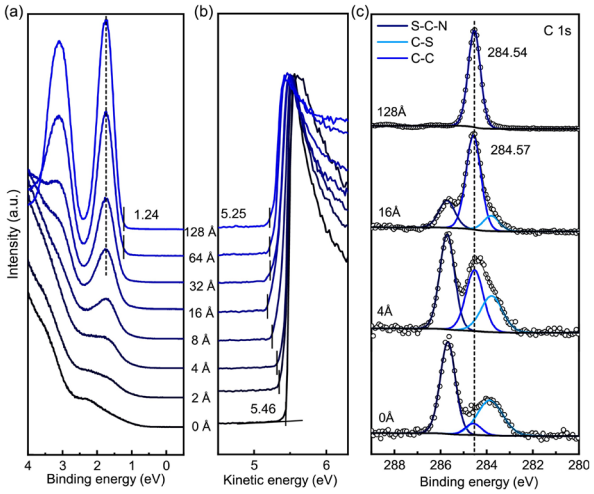

Fig. 4 Thickness-dependent UPS and XPS spectra of C_{60} on CuSCN #xF on ITO: (a) valence band region, (b) secondary electron region, and (c) C 1s core level.

is hampered by overlapping photoemission intensity from CuSCN). The VL slightly decreases from 5.46 eV above E_F for CuSCN #xF with increasing the C_{60} coverage and saturates at 5.25 eV above E_F for a nominally 128 Å thick C_{60} layer (Fig. 4b). The C 1s core level spectra of the C_{60} film with a thickness of 128 Å is centered at 284.54 eV BE and does not show a notable thickness-dependent BE-shift (Fig. 4c). For the highest C_{60} coverage no spectral signatures of CuSCN are apparent, which dominate the 4 Å spectrum and are clearly visible in the 16 Å spectrum. The corresponding C_{60} spectra on the other CuSCN films are shown in Fig. S6.† The C_{60}/CuSCN #Hx spectra are in qualitative agreement with the C_{60}/CuSCN #xF spectra (Fig. 4). The HOMO and the C 1s levels of C_{60} on CuSCN #xx and on CuSCN #HF, however, show thickness-dependent BE-shifts of around 0.10 eV and these parallel shifts, which indicate energy-level bending,[66] will be discussed in more detail below.

Based on the UPS and XPS spectra, we constructed data-based energy-level diagrams,[67] as shown in Fig. 5. The left side of each panel gives the VL, the VBM, and the onset of the gap states of the CuSCN films based on the UPS results in Fig. 2. The optical gaps of the CuSCN films (3.90 eV to 3.95 eV) are used to estimate the position of the conduction band minimum (CBM). In general, the transport gap, which is usually determined by a combination of UPS and inverse photoemission,[68] should be used for this purpose.[69] For inorganic semiconductors, optical and transport gap (which is not reported for CuSCN) are (almost) the same, but for organic semiconductors the differences are in the range of several hundred meV.[70,71] Accordingly, it can be speculated that CuSCN is somewhere in between. The VL and the HOMO-onset of the C_{60} films (right side of each panel) are taken from the respective UPS spectra in Fig. 4 and S6† with a C_{60} thickness of 128 Å. The position of the lowest unoccupied molecular orbital (LUMO) level of the C_{60} films is estimated by using the transport gap (2.30 eV) of solid C_{60}.[72] For the C_{60} films on CuSCN #xx and #HF, the magnitude of energy-level bending is also given, which is determined by the parallel BE-shift of the HOMO and C 1s levels (Fig. S6†). At the interfaces of organic thin films with conductive substrates, such energy-level bending is due to tailing states of the frontier molecular orbital DOS in organic thin film.[54–56] However, at the CuSCN/C_{60} interfaces, such gap states occur at both sides of the interface, which is reminiscent to organic–organic interfaces.[54,73–75] In addition to the energy-level bending at two of the interfaces, an interface dipole, *i.e.*, a shift of the VL upon C_{60} deposition, of around 0.2 eV occurs at all CuSCN/C_{60} interfaces. There are several reasons for such interface dipoles including interfacial ground-state charge transfer, chemical interaction or modification of a surface dipole[66,76] and the latter would point to solution-treatment independent surface-dipole layers of the CuSCN films.

Overall, our data highlights the effect of the solution treatment method on the structural, optical, and electronic properties of spin-coated CuSCN films. As shown by AFM (Fig. 1a), the solution treatment has an eminent impact on the morphology which, in turn, affects the hole transport. CuSCN #xx and CuSCN #Hx films exhibit relatively small, round-like grains and DES adsorption at the grain boundaries does not allow the formation of a notable extended network.[35,36]

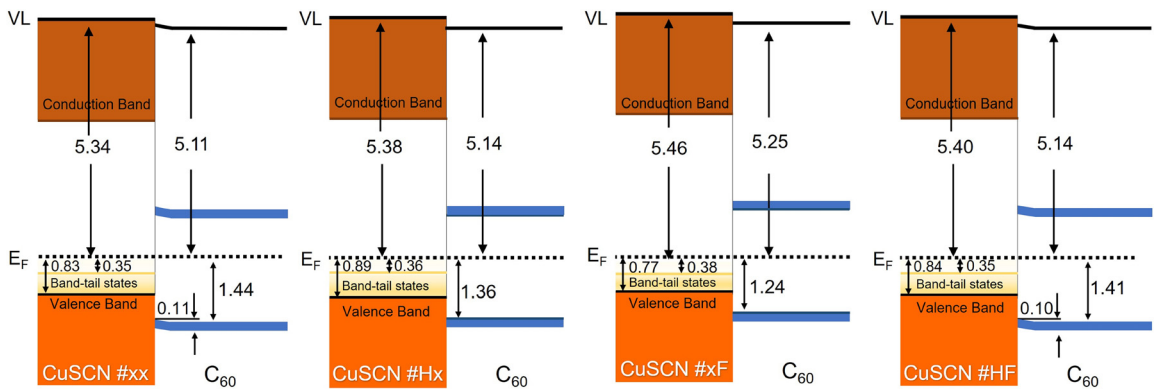

Fig. 5 Schematic energy level diagrams for the C_{60}/CuSCN on ITO interfaces. All values are taken from the UPS and XPS data of this work (Fig. 2, 4 and S6†) as explained in the text.

Filtration of the solution (CuSCN #xF and #HF) leads to larger, ellipsoid-like grains and the surface-coordination of DES and CuSCN allows for the formation of an extended network which favors hole transport.[35,36] The film morphology also has a crucial effect on the electrical properties: CuSCN films with oval/rod-like grains commonly lead to more vertically oriented carrier transport.[32,77,78] Too fast hole transfer will lead to the imbalance of carriers inside the device, hindering the recombination of the CT state carriers at the C_{60}/CuSCN interfaces. In contrast, the mixed film morphology with both oval/rod-like and round-like shapes, as well as the lower defect density, benefit the effective recombination of charge carriers at the interface. Moreover, compared with the flatter and ordered surface of the CuSCN #HF film, the relatively disordered and uneven surface of CuSCN #xF has a larger contact interface area with C_{60}, boosting the generation of CT states. Considering the CT state as a fundamental property of the donor and acceptor heterojunction mixture,[79] while in devices for electroluminescent characterization, the recombination region of excitons will inevitably manifest itself inside a single functional layer,[80] which is the reason for the appearance of emission peaks of C_{60} in Fig. 3. Therefore, the EL peaks in the CT states shown after normalization are in essence the result of a comparison with the emission of C_{60}, which illustrates the better EL performance of CT states in the device with CuSCN #xF due to the above advantages among these four devices. Furthermore, the energy-level diagrams (Fig. 5) show that the VBM onset of CuSCN #xF film is much shallower which provides smoother hole transport though all four CuSCN films with close onsets of band-tail states. The hole injection/transport barrier in CuSCN films can be effectively reduced by solution filtration method. In addition, the wide optical gap of CuSCN (3.92 eV) would give a remarkable exciton blocking ability at the same time.

Conclusion

In summary, we studied the structural, optical, and electronic properties of spin-coated CuSCN films by different solution treatment methods. The morphology depends strongly on the solution treatment method, which further control the CuSCN–DES coordination as revealed by XPS and thus affects hole transport. The optical absorption spectra of CuSCN are not affected by the solution treatment method, all four CuSCN thin films exhibit high transmittance and wide optical gaps. The photoelectron spectroscopy data reveal the electronic structure of CuSCN thin films and the energy-level alignment at C_{60}/CuSCN interfaces. All four CuSCN thin films exhibit band tails states with a similar onset at about 0.35 eV below E_F which contributes to efficient hole transport in the CuSCN film. The solution filtration method can effectively lower the hole transport barrier from anode to CuSCN film, providing a shallower and smoother hole transport pathway. At the interfaces of C_{60}/CuSCN #xx and C_{60}/CuSCN #HF, the broader HOMO DOS and tailing states of the frontier molecular orbital DOS in C_{60} layer lead to energy-level bending in the C_{60} layer. We confirmed the CT states at the C_{60}/CuSCN interface by electroluminescent devices and found that the most prominent EL intensity was exhibited in the one with CuSCN #xF, which was attributed to two main aspects: firstly, based on the SCLC model, the CuSCN #xF device has the lowest density of defect states, which reduces the non-radiative recombination induced by the defects. Secondly, the larger interface area between C_{60} and CuSCN #xF due to mixed crystalline phases is beneficial for more efficient CT states generation. Current studies based on different solution treatment methods open the possibility for further application of CuSCN in various electronic devices.

Methods

Materials

CuSCN (purity 99%, powder) and DES (purity 98%) were purchased from Sigma-Aldrich, C_{60} (purity 99.9%) was purchased from J&K, MoO_3 (purity 99.9%), Ag (purity 99.9999%), Al (purity 99.9999%) were purchased from Alfa Aesar. PEDOT:PSS (Al4083) and BCP were purchased from Xi'an Yuri Solar Co., Ltd.

CuSCN thin film preparation

The ITO substrates were cleaned sequentially with acetone, methanol, and de-ionized (DI) water for 15 min each, and a nitrogen gas flow dried them. CuSCN was dissolved in DES at a concentration of 25 mg ml^{-1} and the solution was stirred overnight before use. The four methods of treating the solution are the solution at room temperature (CuSCN #xx), heating the solution to 60 °C (CuSCN #Hx), filtrating the solution with 0.22 μm PTFE filter (CuSCN #xF), and heating to 60 °C after filtration (CuSCN #HF). The CuSCN thin films were deposited by spin-coating on the ITO substrate from the four solutions described above at 2000 rpm for 40 s, followed by annealing at 100 °C for 10 minutes to remove the excess solvent. All steps were performed in an N_2-filled glove box.

C_{60}/CuSCN heterojunction preparation

C_{60} was thermally evaporated layer-by-layer under ultra-high vacuum conditions (base pressure: 2×10^{-10} bar) on CuSCN thin films from resistively heated cells with deposition rates of about ~3 Å min^{-1} and the thickness of deposited films was monitored by a quartz crystal microbalance positioned near the sample. The values for coverages correspond to nominal film thicknesses.

Device fabrication

Patterned ITO substrates were cleaned with acetone, ethanol, and DI water in sequence. PEDOT:PSS was spin-coated onto plasma-treated ITO at 4000 rpm for 1 min, and then annealed for 30 min at 150 °C. The as-prepared CuSCN solution in DES was then spin-coated on top of the PEDOT:PSS at 5000 rpm for 40 s, followed by annealing at 105 °C for 10 min in the N_2-filled glove box. C_{60} and Al were thermally

evaporated on top of CuSCN under a vacuum pressure of less than 2×10^{-5} bar. For the hole-only devices, MoO_x and Ag were thermally evaporated on top of C_{60}.

Characterization

The crystal structure of thin films was analyzed by an X-ray diffractometer (Bruker D8 Discover) with Cu Kα radiation and the morphology was measured by atomic force microscopy (Veeco MultiMode V). The thickness of CuSCN thin films was measured by measuring the steps of tweezer scratches using AFM and the cross section by scanning electron microscopy (SEM, ZEISS G500) as shown in Fig. S7.† Absorption spectra were acquired by an ultraviolet-visible-near infrared (UV-vis-NIR) spectrometer (Perkin Elmer Lambda 950). A Keithley 2400 SourceMeter and a PhotoResearch spectrometer PR 745 were used for the *I–V* characteristics and the EL spectra of the heterojunction-based devices. XPS (Al Kα, 1486.6 eV) and UPS (He Iα, 21.22 eV) measurements were carried out with monochromatized light sources in a customized SPECS photoelectron spectroscopy system including an analysis chamber (base pressure: 3×10^{-10} bar), an evaporation chamber, and a sample load lock.[81] All CuSCN thin films were transferred from the glovebox to the load lock with an N_2-filled transfer box without being exposed to ambient conditions. The XPS spectra were fitted with a Shirley background and Voigt peaks using CasaXPS software. All preparation steps and measurements were carried out at room temperature (295 K), if not noted otherwise.

Conflicts of interest

There are no conflicts of interest to declare.

Acknowledgements

We thank Shengnan Li for EL measurement. Financial support from the National Natural Science Foundation of China (Grant No. 22150610468), the Collaborative Innovation Center of Suzhou Nano Science & Technology (NANO-CIC), the 111 Project of the Chinese State Administration of Foreign Experts Affairs, the Joint International Research Laboratory of Carbon-Based Functional Materials and Devices, and the Suzhou Key Laboratory of Functional Nano & Soft Materials is gratefully acknowledged.

References

1 A. Kumar, A. Kumar, V. Rao and M. Khajuria, Interfacial Electronic Properties of Hybrid Interfaces, *Mater. Today: Proc.*, 2023, S221478532304796X, DOI: 10.1016/j.matpr.2023.09.125.
2 F. Eisner, G. Foot, J. Yan, M. Azzouzi, D. G. Georgiadou, W. Y. Sit, Y. Firdaus, G. Zhang, Y. Lin, H. Yip, T. D. Anthopoulos and J. Nelson, Emissive Charge-Transfer States at Hybrid Inorganic/Organic Heterojunctions Enable Low Non-Radiative Recombination and High-Performance Photodetectors, *Adv. Mater.*, 2022, **34**(22), 2104654, DOI: 10.1002/adma.202104654.
3 N. Koch, Opportunities for Energy Level Tuning at Inorganic/Organic Semiconductor Interfaces, *Appl. Phys. Lett.*, 2021, **119**(26), 260501, DOI: 10.1063/5.0074963.
4 O. T. Hofmann, E. Zojer, L. Hörmann, A. Jeindl and R. J. Maurer, First-Principles Calculations of Hybrid Inorganic–Organic Interfaces: From State-of-the-Art to Best Practice, *Phys. Chem. Chem. Phys.*, 2021, **23**(14), 8132–8180, DOI: 10.1039/D0CP06605B.
5 H. Liu, Q. Liu, J. Liu, Y. Zhao, Y. Yu, Y. An, G. Wei, Y. Li, Y. Fu, J. Li and D. He, Effects of Different Interface on the Stability of Hybrid Heterojunction Solar Cells, *Sol. Energy Mater. Sol. Cells*, 2024, **264**, 112624, DOI: 10.1016/j.solmat.2023.112624.
6 S.-S. Li and C.-W. Chen, Polymer–Metal-Oxide Hybrid Solar Cells, *J. Mater. Chem. A*, 2013, **1**(36), 10574, DOI: 10.1039/c3ta11998j.
7 X. Fan, M. Zhang, X. Wang, F. Yang and X. Meng, Recent Progress in Organic–Inorganic Hybrid Solar Cells, *J. Mater. Chem. A*, 2013, **1**(31), 8694, DOI: 10.1039/c3ta11200d.
8 M. Wright and A. Uddin, Organic—Inorganic Hybrid Solar Cells: A Comparative Review, *Sol. Energy Mater. Sol. Cells*, 2012, **107**, 87–111, DOI: 10.1016/j.solmat.2012.07.006.
9 J. Niederhausen, K. A. Mazzio and R. W. MacQueen, Inorganic–Organic Interfaces in Hybrid Solar Cells, *Electron. Struct.*, 2021, **3**(3), 033002, DOI: 10.1088/2516-1075/ac23a3.
10 P. Pattanasattayavong, G. O. N. Ndjawa, K. Zhao, K. W. Chou, N. Yaacobi-Gross, B. C. O'Regan, A. Amassian and T. D. Anthopoulos, Electric Field-Induced Hole Transport in Copper(i) Thiocyanate (CuSCN) Thin-Films Processed from Solution at Room Temperature, *Chem. Commun.*, 2013, **49**(39), 4154–4156, DOI: 10.1039/C2CC37065D.
11 P. Pattanasattayavong, N. Yaacobi-Gross, K. Zhao, G. O. N. Ndjawa, J. Li, F. Yan, B. C. O'Regan, A. Amassian and T. D. Anthopoulos, Hole-Transporting Transistors and Circuits Based on the Transparent Inorganic Semiconductor Copper(I) Thiocyanate (CuSCN) Processed from Solution at Room Temperature, *Adv. Mater.*, 2013, **25**(10), 1504–1509, DOI: 10.1002/adma.201202758.
12 P. Pattanasattayavong, A. D. Mottram, F. Yan and T. D. Anthopoulos, Study of the Hole Transport Processes in Solution-Processed Layers of the Wide Bandgap Semiconductor Copper(I) Thiocyanate (CuSCN), *Adv. Funct. Mater.*, 2015, **25**(43), 6802–6813, DOI: 10.1002/adfm.201502953.
13 N. Yaacobi-Gross, N. D. Treat, P. Pattanasattayavong, H. Faber, A. K. Perumal, N. Stingelin, D. D. C. Bradley, P. N. Stavrinou, M. Heeney and T. D. Anthopoulos, High-Efficiency Organic Photovoltaic Cells Based on the Solution-Processable Hole Transporting Interlayer Copper Thiocyanate (CuSCN) as a Replacement for PEDOT:PSS, *Adv. Energy Mater.*, 2015, **5**(3), 1401529, DOI: 10.1002/aenm.201401529.
14 A. Perumal, H. Faber, N. Yaacobi-Gross, P. Pattanasattayavong, C. Burgess, S. Jha, M. A. McLachlan, P. N. Stavrinou, T. D. Anthopoulos and D. D. C. Bradley, High-Efficiency, Solution-Processed, Multilayer Phosphorescent Organic Light-Emitting Diodes with a Copper Thiocyanate Hole-Injection/Hole-Transport Layer, *Adv. Mater.*, 2015, **27**(1), 93–100, DOI: 10.1002/adma.201403914.

15 K. Tennakone, A. H. Jayatissa, C. a. N. Fernando, S. Wickramanayake, S. Punchihewa, L. K. Weerasena and W. D. R. Premasiri, Semiconducting and Photoelectrochemical Properties of N- and p-Type β-CuCNS, *Phys. Status Solidi A*, 1987, **103**(2), 491–497, DOI: **10.1002/pssa.2211030220**.

16 J. E. Jaffe, T. C. Kaspar, T. C. Droubay, T. Varga, M. E. Bowden and G. J. Exarhos, Electronic and Defect Structures of CuSCN, *J. Phys. Chem. C*, 2010, **114**(19), 9111–9117, DOI: **10.1021/jp101586q**.

17 A. Perumal, H. Faber, N. Yaacobi-Gross, P. Pattanasattayavong, C. Burgess, S. Jha, M. A. McLachlan, P. N. Stavrinou, T. D. Anthopoulos and D. D. C. Bradley, High-Efficiency, Solution-Processed, Multilayer Phosphorescent Organic Light-Emitting Diodes with a Copper Thiocyanate Hole-Injection/Hole-Transport Layer, *Adv. Mater.*, 2015, **27**(1), 93–100, DOI: **10.1002/adma.201403914**.

18 N. Thejo Kalyani and S. J. Dhoble, Organic Light Emitting Diodes: Energy Saving Lighting Technology—A Review, *Renewable Sustainable Energy Rev.*, 2012, **16**(5), 2696–2723, DOI: **10.1016/j.rser.2012.02.021**.

19 B. C. O'Regan and F. Lenzmann, Charge Transport and Recombination in a Nanoscale Interpenetrating Network of N-Type and p-Type Semiconductors: Transient Photocurrent and Photovoltage Studies of TiO_2/Dye/CuSCN Photovoltaic Cells, *J. Phys. Chem. B*, 2004, **108**(14), 4342–4350, DOI: **10.1021/jp035613n**.

20 J. W. Jung, C.-C. Chueh and A. K.-Y. Jen, High-Performance Semitransparent Perovskite Solar Cells with 10% Power Conversion Efficiency and 25% Average Visible Transmittance Based on Transparent CuSCN as the Hole-Transporting Material, *Adv. Energy Mater.*, 2015, **5**(17), 1500486, DOI: **10.1002/aenm.201500486**.

21 P. Qin, S. Tanaka, S. Ito, N. Tetreault, K. Manabe, H. Nishino, M. K. Nazeeruddin and M. Grätzel, Inorganic Hole Conductor-Based Lead Halide Perovskite Solar Cells with 12.4% Conversion Efficiency, *Nat. Commun.*, 2014, **5**(1), 3834, DOI: **10.1038/ncomms4834**.

22 K. Nakano, Y. Chen, B. Xiao, W. Han, J. Huang, H. Yoshida, E. Zhou and K. Tajima, Anatomy of the Energetic Driving Force for Charge Generation in Organic Solar Cells, *Nat. Commun.*, 2019, **10**(1), 2520, DOI: **10.1038/s41467-019-10434-3**.

23 D. Xue, Q. Wang, M. Xie, W. Gong, Y. Zhang, Y. Yin, Y. Wei, J. Lu, J. Zhang, S. Duhm, Z. Wang, L. Chi and L. Huang, Tunable Light Response Modulated by the Organic Interface Charge Transfer Effect, *Adv. Opt. Mater.*, 2023, 2302091, DOI: **10.1002/adom.202302091**.

24 A. Jungbluth, P. Kaienburg and M. Riede, Charge Transfer State Characterization and Voltage Losses of Organic Solar Cells, *JPhys Mater.*, 2022, **5**(2), 024002, DOI: **10.1088/2515-7639/ac44d9**.

25 V. Coropceanu, X.-K. Chen, T. Wang, Z. Zheng and J.-L. Brédas, Charge-Transfer Electronic States in Organic Solar Cells, *Nat. Rev. Mater.*, 2019, **4**(11), 689–707, DOI: **10.1038/s41578-019-0137-9**.

26 S. R. Forrest, *Organic Electronics: Foundations to Applications*, Oxford University PressOxford, 1st edn, 2020, DOI: **10.1093/oso/9780198529729.001.0001**.

27 S. Park, T. Kim, S. Yoon, C. W. Koh, H. Y. Woo and H. J. Son, Progress in Materials, Solution Processes, and Long-Term Stability for Large-Area Organic Photovoltaics, *Adv. Mater.*, 2020, **32**(51), 2002217, DOI: **10.1002/adma.202002217**.

28 Y. Zhang, Q. Wang, F. Hu, Y. Wang, D. Wu, R. Wang and S. Duhm, Photoelectron Spectroscopy Reveals the Impact of Solvent Additives on Poly(3,4-Ethylenedioxythiophene): Poly(Styrenesulfonate) Thin Film Formation, *ACS Phys. Chem. Au*, 2023, **3**(3), 311–319, DOI: **10.1021/acsphyschemau.2c00073**.

29 G. R. R. A. Kumara, A. Konno, G. K. R. Senadeera, P. V. V. Jayaweera, D. B. R. A. De Silva and K. Tennakone, Dye-Sensitized Solar Cell with the Hole Collector p-CuSCN Deposited from a Solution in n-Propyl Sulphide, *Sol. Energy Mater. Sol. Cells*, 2001, **69**(2), 195–199, DOI: **10.1016/S0927-0248(01)00027-7**.

30 G. Murugadoss, R. Thangamuthu and S. M. Senthil Kumar, Fabrication of CH3NH3PbI3 Perovskite-Based Solar Cells: Developing Various New Solvents for CuSCN Hole Transport Material, *Sol. Energy Mater. Sol. Cells*, 2017, **164**, 56–62, DOI: **10.1016/j.solmat.2017.02.011**.

31 F. Hilpert, P.-C. Liao, E. Franz, V. M. Koch, L. Fromm, E. Topraksal and A. Görling, Mechanistic Insight into Solution-Based Atomic Layer Deposition of CuSCN Provided by In Situ and Ex Situ Methods, *ACS Appl. Mater. Interfaces*, 2023, **15**(15), 19536–19544, DOI: **10.1021/acsami.2c16943**.

32 N. Chaudhary, S. Naqvi, D. Rathore, S. Rathi and A. Patra, Solvent Influenced Morphology Control of Hole Transport Layer of CuSCN on Performance of Organic Solar Cells, *Mater. Chem. Phys.*, 2022, **282**, 125898, DOI: **10.1016/j.matchemphys.2022.125898**.

33 N. Wijeyasinghe and T. D. Anthopoulos, Copper(I) Thiocyanate (CuSCN) as a Hole-Transport Material for Large-Area Opto/Electronics, *Semicond. Sci. Technol.*, 2015, **30**(10), 104002, DOI: **10.1088/0268-1242/30/10/104002**.

34 K. M. Miller, S. M. McCullough, E. A. Lepekhina, I. J. Thibau, R. D. Pike, X. Li, J. P. Killarney and H. H. Patterson, Copper(I) Thiocyanate-Amine Networks: Synthesis, Structure, and Luminescence Behavior, *Inorg. Chem.*, 2011, **50**(15), 7239–7249, DOI: **10.1021/ic200821f**.

35 P. Worakajit, F. Hamada, D. Sahu, P. Kidkhunthod, T. Sudyoadsuk, V. Promarak, D. J. Harding, D. M. Packwood, A. Saeki and P. Pattanasattayavong, Elucidating the Coordination of Diethyl Sulfide Molecules in Copper(I) Thiocyanate (CuSCN) Thin Films and Improving Hole Transport by Antisolvent Treatment, *Adv. Funct. Mater.*, 2020, **30**(36), 2002355, DOI: **10.1002/adfm.202002355**.

36 P. Pattanasattayavong, D. M. Packwood and D. J. Harding, Structural Versatility and Electronic Structures of Copper(I) Thiocyanate (CuSCN)–Ligand Complexes, *J. Mater. Chem. C*, 2019, **7**(41), 12907–12917, DOI: **10.1039/C9TC03198G**.

37 X.-D. Gao, X.-M. Li, W.-D. Yu, J.-J. Qiu and X.-Y. Gan, Room-Temperature Deposition of Nanocrystalline CuSCN Film by the Modified Successive Ionic Layer Adsorption and Reaction Method, *Thin Solid Films*, 2008, **517**(2), 554–559, DOI: **10.1016/j.tsf.2008.06.077**.

38 W. Wu, Z. Jin, Z. Hua, Y. Fu and J. Qiu, Growth Mechanisms of CuSCN Films Electrodeposited on ITO in EDTA-Chelated

Copper(II) and KSCN Aqueous Solution, *Electrochim. Acta*, 2005, **50**(11), 2343–2349, DOI: **10.1016/j.electacta.2004.10.048**.

39 Y. Ni, Z. Jin and Y. Fu, Electrodeposition of P-Type CuSCN Thin Films by a New Aqueous Electrolyte With Triethanolamine Chelation, *J. Am. Ceram. Soc.*, 2007, **90**(9), 2966–2973, DOI: **10.1111/j.1551-2916.2007.01832.x**.

40 C. Ronning, H. Feldermann, R. Merk, H. Hofsäss, P. Reinke and J.-U. Thiele, Carbon Nitride Deposited Using Energetic Species: A Review on XPS Studies, *Phys. Rev. B: Condens. Matter Mater. Phys.*, 1998, **58**(4), 2207–2215, DOI: **10.1103/PhysRevB.58.2207**.

41 A. Regoutz, M. S. Wolinska, N. K. Fernando and L. E. Ratcliff, A Combined Density Functional Theory and X-Ray Photoelectron Spectroscopy Study of the Aromatic Amino Acids, *Electron. Struct.*, 2020, **2**(4), 044005, DOI: **10.1088/2516-1075/abd63c**.

42 G. Greczynski and L. Hultman, X-Ray Photoelectron Spectroscopy: Towards Reliable Binding Energy Referencing, *Prog. Mater. Sci.*, 2020, **107**, 100591, DOI: **10.1016/j.pmatsci.2019.100591**.

43 M. C. Biesinger, Advanced Analysis of Copper X-Ray Photoelectron Spectra, *Surf. Interface Anal.*, 2017, **49**(13), 1325–1334, DOI: **10.1002/sia.6239**.

44 D. Aldakov, C. Chappaz-Gillot, R. Salazar, V. Delaye, K. A. Welsby, V. Ivanova and P. R. Dunstan, Properties of Electrodeposited CuSCN 2D Layers and Nanowires Influenced by Their Mixed Domain Structure, *J. Phys. Chem. C*, 2014, **118**(29), 16095–16103, DOI: **10.1021/jp412499f**.

45 N. Wijeyasinghe, A. Regoutz, F. Eisner, T. Du, L. Tsetseris, Y.-H. Lin, H. Faber, P. Pattanasattayavong, J. Li, F. Yan, M. A. McLachlan, D. J. Payne, M. Heeney and T. D. Anthopoulos, Copper(I) Thiocyanate (CuSCN) Hole-Transport Layers Processed from Aqueous Precursor Solutions and Their Application in Thin-Film Transistors and Highly Efficient Organic and Organometal Halide Perovskite Solar Cells, *Adv. Funct. Mater.*, 2017, **27**(35), 1701818, DOI: **10.1002/adfm.201701818**.

46 I. S. Jin, J. H. Lee, Y. W. Noh, S. H. Park and J. W. Jung, Molecular Doping of CuSCN for Hole Transporting Layers in Inverted-Type Planar Perovskite Solar Cells, *Inorg. Chem. Front.*, 2019, **6**(8), 2158–2166, DOI: **10.1039/C9QI00557A**.

47 G. Greczynski and L. Hultman, A Step-by-Step Guide to Perform x-Ray Photoelectron Spectroscopy, *J. Appl. Phys.*, 2022, **132**(1), 011101, DOI: **10.1063/5.0086359**.

48 T. Schultz, A Unified Secondary Electron Cut-off Presentation and Common Mistakes in Photoelectron Spectroscopy, *Electron. Struct.*, 2022, **4**(4), 044002, DOI: **10.1088/2516-1075/ac9ffb**.

49 K. Tennakone, A. H. Jayatissa, C. a. N. Fernando, S. Wickramanayake, S. Punchihewa, L. K. Weerasena and W. D. R. Premasiri, Semiconducting and Photoelectrochemical Properties of N- and p-Type β-CuCNS, *Phys. Status Solidi A*, 1987, **103**(2), 491–497, DOI: **10.1002/pssa.2211030220**.

50 W. Ji, G.-Q. Yue, F.-S. Ke, S. Wu, H.-B. Zhao, L.-Y. Chen, S.-Y. Wang and Y. Jia, Electronic Structures and Optical Properties of CuSCN with Cu Vacancies, *J. Korean Phys. Soc.*, 2012, **60**(8), 1253–1257, DOI: **10.3938/jkps.60.1253**.

51 M. Kim, S. Park, J. Jeong, D. Shin, J. Kim, S. H. Ryu, K. S. Kim, H. Lee and Y. Yi, Band-Tail Transport of CuSCN: Origin of Hole Extraction Enhancement in Organic Photovoltaics, *J. Phys. Chem. Lett.*, 2016, **7**(14), 2856–2861, DOI: **10.1021/acs.jpclett.6b01039**.

52 P. Pattanasattayavong, V. Promarak and T. D. Anthopoulos, Electronic Properties of Copper(I) Thiocyanate (CuSCN), *Adv. Electron. Mater.*, 2017, **3**(3), 1600378, DOI: **10.1002/aelm.201600378**.

53 W. Ji, G.-Q. Yue, F.-S. Ke, S. Wu, H.-B. Zhao, L.-Y. Chen, S.-Y. Wang and Y. Jia, Electronic Structures and Optical Properties of CuSCN with Cu Vacancies, *J. Korean Phys. Soc.*, 2012, **60**(8), 1253–1257, DOI: **10.3938/jkps.60.1253**.

54 M. Oehzelt, N. Koch and G. Heimel, Organic Semiconductor Density of States Controls the Energy Level Alignment at Electrode Interfaces, *Nat. Commun.*, 2014, **5**(1), 4174, DOI: **10.1038/ncomms5174**.

55 J.-P. Yang, F. Bussolotti, S. Kera and N. Ueno, Origin and Role of Gap States in Organic Semiconductor Studied by UPS: As the Nature of Organic Molecular Crystals, *J. Phys. D: Appl. Phys.*, 2017, **50**(42), 423002, DOI: **10.1088/1361-6463/aa840f**.

56 L. Zhang, M. Berteau-Rainville, T. Zhai, Y. Wang, Q. Wang, I. Salzmann and S. Duhm, Chemical Defects and Energetic Disorder Impact the Energy-Level Alignment of Functionalized Hexaazatriphenylene Thin Films, *Phys. Status Solidi RRL*, 2023, **17**(9), 2300001, DOI: **10.1002/pssr.202300001**.

57 S. Jung, C.-H. Kim, Y. Bonnassieux and G. Horowitz, Injection Barrier at Metal/Organic Semiconductor Junctions with a Gaussian Density-of-States, *J. Phys. D: Appl. Phys.*, 2015, **48**(39), 395103, DOI: **10.1088/0022-3727/48/39/395103**.

58 F. D. Eisner, M. Azzouzi, Z. Fei, X. Hou, T. D. Anthopoulos, T. J. S. Dennis, M. Heeney and J. Nelson, Hybridization of Local Exciton and Charge-Transfer States Reduces Nonradiative Voltage Losses in Organic Solar Cells, *J. Am. Chem. Soc.*, 2019, **141**(15), 6362–6374, DOI: **10.1021/jacs.9b01465**.

59 G.-J. A. H. Wetzelaer, M. Kuik and P. W. M. Blom, Identifying the Nature of Charge Recombination in Organic Solar Cells from Charge-Transfer State Electroluminescence, *Adv. Energy Mater.*, 2012, **2**(10), 1232–1237, DOI: **10.1002/aenm.201200009**.

60 C. M. Proctor, M. Kuik and T.-Q. Nguyen, Charge Carrier Recombination in Organic Solar Cells, *Prog. Polym. Sci.*, 2013, **38**(12), 1941–1960, DOI: **10.1016/j.progpolymsci.2013.08.008**.

61 R. H. Bube, Trap Density Determination by Space-Charge-Limited Currents, *J. Appl. Phys.*, 1962, **33**(5), 1733–1737, DOI: **10.1063/1.1728818**.

62 T. Zhai, R. Wang, T. Katase, F. Quigley, H. Ohta, P. Amsalem, N. Koch and S. Duhm, Substrate-Independent Energy-Level Pinning of an Organic Semiconductor Providing Versatile Hole-Injection Electrodes, *ACS Appl. Electron. Mater.*, 2020, **2**(12), 3994–4001, DOI: **10.1021/acsaelm.0c00823**.

63 E. Manousakis, Electronic Structure of C 60 within the Tight-Binding Approximation, *Phys. Rev. B: Condens. Matter Mater. Phys.*, 1991, **44**(19), 10991–10994, DOI: **10.1103/PhysRevB.44.10991**.

64 K. Andersson, The Electronic Spectrum of C60, *Chem. Phys. Lett.*, 2020, **739**, 136976, DOI: **10.1016/j.cplett.2019.136976**.

65 I. Salzmann, S. Duhm, R. Opitz, R. L. Johnson, J. P. Rabe and N. Koch, Structural and Electronic Properties of pentacene-Fullerene Heterojunctions, *J. Appl. Phys.*, 2008, **104**(11), 114518, DOI: **10.1063/1.3040003**.

66 Q. Wang, J. Yang, A. Gerlach, F. Schreiber and S. Duhm, Advanced Characterization of Organic–Metal and Organic–Organic Interfaces: From Photoelectron Spectroscopy Data to Energy-Level Diagrams, *JPhys Mater.*, 2022, **5**(4), 044010, DOI: **10.1088/2515-7639/ac9f6f**.

67 S. Duhm, Interface Energetics Make Devices, *Electron. Struct.*, 2022, **4**(3), 034003, DOI: **10.1088/2516-1075/ac884d**.

68 D. R. T. Zahn, G. N. Gavrila and M. Gorgoi, The Transport Gap of Organic Semiconductors Studied Using the Combination of Direct and Inverse Photoemission, *Chem. Phys.*, 2006, **325**(1), 99–112, DOI: **10.1016/j.chemphys.2006.02.003**.

69 J.-L. Bredas, Mind the Gap!, *Mater. Horiz.*, 2014, **1**(1), 17–19, DOI: **10.1039/C3MH00098B**.

70 J. Bertrandie, J. Han, C. S. P. De Castro, E. Yengel, J. Gorenflot, T. Anthopoulos, F. Laquai, A. Sharma and D. Baran, The Energy Level Conundrum of Organic Semiconductors in Solar Cells, *Adv. Mater.*, 2022, **34**(35), 2202575, DOI: **10.1002/adma.202202575**.

71 S. R. Forrest, Excitons and the Lifetime of Organic Semiconductor Devices, *Philos. Trans. R. Soc., A*, 2015, **373**(2044), 20140320, DOI: **10.1098/rsta.2014.0320**.

72 R. W. Lof, M. A. Van Veenendaal, B. Koopmans, H. T. Jonkman and G. A. Sawatzky, Band Gap, Excitons, and Coulomb Interaction in Solid C 60, *Phys. Rev. Lett.*, 1992, **68**(26), 3924–3927, DOI: **10.1103/PhysRevLett.68.3924**.

73 M. Oehzelt, K. Akaike, N. Koch and G. Heimel, Energy-Level Alignment at Organic Heterointerfaces, *Sci. Adv.*, 2015, **1**(10), e1501127, DOI: **10.1126/sciadv.1501127**.

74 F. Bussolotti, J. Yang, A. Hinderhofer, Y. Huang, W. Chen, S. Kera, A. T. S. Wee and N. Ueno, Origin of the Energy Level Alignment at Organic/Organic Interfaces: The Role of Structural Defects, *Phys. Rev. B: Condens. Matter Mater. Phys.*, 2014, **89**(11), 115319, DOI: **10.1103/PhysRevB.89.115319**.

75 A. Opitz, Energy Level Alignment at Planar Organic Heterojunctions: Influence of Contact Doping and Molecular Orientation, *J. Phys.: Condens. Matter*, 2017, **29**(13), 133001, DOI: **10.1088/1361-648X/aa5a6c**.

76 H. Ishii, K. Sugiyama, E. Ito and K. Seki, Energy Level Alignment and Interfacial Electronic Structures at Organic/Metal and Organic/Organic Interfaces, *Adv. Mater.*, 1999, **11**(8), 605–625, DOI: **10.1002/(SICI)1521-4095(199906)11:8<605::AID-ADMA605>3.0.CO;2-Q**.

77 Q. Xi, G. Gao, H. Zhou, Y. Zhao, C. Wu, L. Wang, P. Guo and J. Xu, Highly Efficient Inverted Solar Cells Based on Perovskite Grown Nanostructures Mediated by CuSCN, *Nanoscale*, 2017, **9**(18), 6136–6144, DOI: **10.1039/C7NR01135K**.

78 J. W. Jung, C.-C. Chueh and A. K.-Y. Jen, High-Performance Semitransparent Perovskite Solar Cells with 10% Power Conversion Efficiency and 25% Average Visible Transmittance Based on Transparent CuSCN as the Hole-Transporting Material, *Adv. Energy Mater.*, 2015, **5**(17), 1500486, DOI: **10.1002/aenm.201500486**.

79 M. List, T. Sarkar, P. Perkhun, J. Ackermann, C. Luo and U. Würfel, Correct Determination of Charge Transfer State Energy from Luminescence Spectra in Organic Solar Cells, *Nat. Commun.*, 2018, **9**(1), 3631, DOI: **10.1038/s41467-018-05987-8**.

80 R. Lampande, A. Pizano, M. Gui, R. Cawthorn, B. P. Rand and N. C. Giebink, Dispersive Charge Transfer State Electroluminescence in Organic Solar Cells, *Adv. Energy Mater.*, 2023, **13**(24), 2300394, DOI: **10.1002/aenm.202300394**.

81 M.-C. Lu, R.-B. Wang, A. Yang and S. Duhm, pentacene on Au(1 1 1), Ag(1 1 1) and Cu(1 1 1): From Physisorption to Chemisorption, *J. Phys.: Condens. Matter*, 2016, **28**(9), 094005, DOI: **10.1088/0953-8984/28/9/094005**.